Supplementary Information (SI) for Materials Horizons.

Supplementary Materials for

Suppressing Thermal Transport in Nonporous Polymer Hybrids by Limiting Thermally Accessible Vibrational Modes

Henry Worden,[1#] Mihir Chandra,[1,2#] Yijie Zhou,[1#] Zarif Ahmad Razin Bhuiyan,[3] Mouyang Cheng,[4] Krishnamurthy Munusamy,[5] Duc Nghiem,[1] Weiguo Hu,[5] Weibo Yan,[1] Siyu Wu,[6] Ruipeng Li,[6] Zhang Jiang,[7] Anna Chatterji,[1] Shengjia Zhang,[8] Ilia N. Ivanov,[9] Jihua Chen,[9] Jack C Lasseter,[9] Mengru Jin,[8] Derin Abitagaoglu,[8] Qing Tu,[8] Todd Emrick,[5] Jun Liu,[3] Yanfei Xu[1,2*]

1. Department of Mechanical and Industrial Engineering, University of Massachusetts, Amherst, Massachusetts, 01003, United States of America
2. Department of Material Science and Engineering, University of Massachusetts, Amherst, Massachusetts, 01003, United States of America
3. Department of Mechanical and Aerospace Engineering, North Carolina State University, Raleigh, NC 27695, USA.
4. Department of Materials Science and Engineering, Massachusetts Institute of Technology, Cambridge, MA 02139, USA.
5. Department of Polymer Science and Engineering, University of Massachusetts, Amherst, Massachusetts, 01003, United States of America
6. Brookhaven National Laboratory, Upton, New York, 11973, United States of America
7. Advanced Photon Source, Argonne National Laboratory, Argonne, IL 60439, USA.
8. Department of Materials Science and Engineering, Texas A&M University, College Station, TX 77843
9. Center for Nanophase Materials Sciences, Oak Ridge National Laboratory, Oak Ridge, TN 37831, USA.

#Contribute equally

[*] Corresponding author yanfeixu@umass.edu

Supplementary Materials

This file includes:

- **Section S1.** Sample preparation
- **Section S2.** Experimental characterization and error analysis
- **Section S3.** Molecular dynamics simulations of thermal transport in polymer/filler hybrids
- **Section 4.** Applicability and limitations of effective medium theory for THDBT/PU hybrids
- **Section S5.** Effective Hamiltonian model for polymer thermal transport with fillers

Figures S1–S10
Tables S1-S2
References

Section S1. Sample preparation, experimental characterization, and error analysis.

Section S1.1 Sample preparations.

Preparation of PU solution and pure PU thin films.

A solution containing $7\ wt\%$ of PU was prepared using DMF as solvent. PU ($0.2\ g$) was added into DMF ($2.67\ g$) in a $20\ mL$ glass vial. The temperature of the mixture was then raised to $\sim 75\ °C$ using an oil bath and stirred for 6 hours until the PU was completely dissolved. The solution was then poured into a silicone mold ($100\ mm \times 20\ mm$) and dried in an oven at $75\ °C$ for 24 hours. The sample was further dried under vacuum at $120\ °C$ for 2 hours to fully remove the DMF. The final PU film with thickness of $\sim 80\ \mu m$ was peeled off the silicone mold after the drying process completed.

Preparation of tetrahydroxy deoxybenzoins triazole (THDBT).

The detailed synthesis of THDBT has been described in the recent publication.[1] Briefly, the synthesis involves a two-step process:

(1) Preparation of tetramethoxy deoxybenzoins triazole.

1,4-Bis(azidomethyl)benzene ($2.00\ g, 10.6\ mmol$) and alkynyl desoxyanisoin (7 .80 $g, 26.6\ mmol$) were reacted in tetrahydrofuran (THF, $20\ mL$) under nitrogen. An aqueous solution of sodium ascorbate and $CuSO_4 \cdot 5H_2O$ was added. The mixture was heated at $30\ °C$ for 12 hours, then extracted with dichloromethane. The organic layer was dried over magnesium sulfate, filtered, and concentrated. The crude product was purified to yield tetramethoxy deoxybenzoins triazole as a yellow powder and was confirmed by ^1H and ^{13}C NMR spectroscopy.

(2) Conversion to THDBT.

Tetramethoxy deoxybenzoins triazole ($5.00\ g, 6.43\ mmol$) was treated with hydroiodic acid ($14\ mL$) in glacial acetic acid (*10 mL*) at 140 °C for 7 hours. After cooling, the mixture was poured into water to precipitate THDBT, which was then filtered and dried. Finally, the compound was confirmed by ^1H and ^{13}C NMR spectroscopy.[1]

Preparation of samples for thermal diffusivity measurements.

(1) Preparation of compressed pellets of THDBT fillers for thermal diffusivity measurements.

To measure the cross-plane thermal diffusivity of THDBT fillers, compressed pellets of THDBT fillers are prepared using the following procedure. The THDBT powder is weighed out ($\sim 0.7\ g$) as per experimental design and is poured into a customized mold with a diameter of 12.7 mm. A pressure of 58 MPa is applied to the mold using a hydraulic press for 3 minutes to form the pellet specimen (thickness $\sim 0.7\ mm$). The compressed pellets of THDBT fillers are then sprayed with graphite (DGF 123, Miracle Power Products) prior to measuring cross-plane thermal diffusivities.

(2) Preparation of pure PU films for thermal diffusivity measurements.

PU/THDBT hybrid films with THDBT volume fractions of 4.5, 13.9, and $23.3\ vol\%$ were prepared via a solution blending method. As a representative example, the preparation of a film containing $23.3\ vol\%$ THDBT is described. THDBT ($0.067\ g$) and PU ($0.200\ g$) were placed in a $20\ mL$ glass vial, followed by the addition of N,N-dimethylformamide (DMF, $2.670\ g$) as the solvent. The mixture was heated to $\sim 75\ ^{\circ}C$ in an oil bath and magnetically stirred for 6 h until the PU was completely dissolved, forming a homogeneous PU/THDBT solution. The solution was then cast into a silicone mold ($100\ mm\ \times\ 20\ mm$) and dried in an oven at $75\ ^{\circ}C$ for 24 hours, followed by vacuum drying at $120\ ^{\circ}C$ for 12 hours. After drying, a flexible hybrid film (~100 μm thick) was obtained by peeling it from the mold.

(3) Preparation of pure PU films for thermal diffusivity measurements.

To measure the cross-plane thermal diffusivity of pure PU films, samples are prepared as follows. PU ($0.2\ g$) was dissolved in N,N-dimethylformamide (DMF, $2.67\ g$) in a $20\ mL$ glass vial. The mixture was heated to $\sim 75\ ^{\circ}C$ in an oil bath and stirred for 6 hours until the PU was completely dissolved. The resulting solution was cast into a silicone mold ($100\ mm\ \times\ 20\ mm$) and dried in an oven at $75\ ^{\circ}C$ for 24 hours, followed by vacuum drying at $120\ ^{\circ}C$ for 2 hours to remove residual solvent. The obtained PU film ($\sim 80\ \mu m$ thickness) was removed from the mold and cut into circular specimens ($12.7\ mm$ in diameter) using a hollow punch.

Preparation of samples for X-ray scattering measurements.

(1) Preparation of PU thin films for X-ray scattering measurements.

Samples were prepared using the same procedure as those used for the thermal diffusivity measurements.

(2) Preparation of PU/THDBT hybrids for X-ray scattering measurements.

Samples were prepared using the same procedure as those used for the thermal diffusivity measurements.

(3) Preparation of compressed pellets of THDBT fillers for X-ray scattering measurements.

Samples were prepared using the same procedure as those used for the thermal diffusivity measurements.

Preparation of samples for Attenuated total reflectance fourier transform infrared (ATR-FTIR) spectroscopic analysis

(1) Preparation of PU thin films for ATR-FTIR spectroscopic analysis (Figure 5D).

Samples were prepared using the same procedure as those used for the thermal diffusivity measurements.

(2) Preparation of PU/THDBT hybrids for ATR-FTIR spectroscopic analysis (Figure 5D).

Samples were prepared using the same procedure as those used for the thermal diffusivity measurements.

(3) Preparation of compressed pellets of THDBT fillers for ATR-FTIR spectroscopic analysis (Figure 5D).

Samples were prepared using the same procedure as those used for the thermal diffusivity measurements.

(4) Preparation of THDBT fillers for ATR-FTIR spectroscopic analysis (Figure S8).

Approximately $24\ mg$ of THDBT powder was mixed with $71\ mg$ of potassium bromide (KBr) and finely ground to ensure homogeneity. The mixture was then loaded into a custom mold (12.7 mm in diameter) and pressed at 4$6\ MPa$ for 1 minute using a hydraulic press to form pellet specimens.

Section S2. Experimental characterization and error analysis

Section S2.1 Experimental characterizations and instrumental measurement details

Thermal diffusivity measurements.

(1) Cross-plane thermal diffusivities of pure PU films and PU/THDBT hybrid (films) measured using a laser flash apparatus (LFA 467 HyperFlash, NETZSCH). The instrument is operated with a lamp voltage of $150\ V$ and a pulse width of $50\ \mu s$. Prior to measurement, both sides of each sample (prepared as described in Section S1.1) were coated with graphite spray (DGF 123, Miracle Power Products) and allowed to dry at room temperature for $5\ minutes$.[2] Prior to measurement, all samples were equilibrated at $298\ K$. For PU films and PU/THDBT hybrid films, the transparent model in the NETZSCH analysis software is applied to evaluate the laser flash data and determine the thermal diffusivity.[2]

(2) Cross-plane thermal diffusivities of compressed pellets of THDBT fillers

The cross-plane thermal diffusivities of the compressed pellets of THDBT fillers are measured using a laser flash apparatus (LFA 467 HyperFlash, NETZSCH). The instrument is operated with a lamp voltage of $250\ V$ and a pulse width of $600\ \mu s$. Prior to measurement, both sides of each sample (prepared as described in Section S1.1) were coated with graphite spray (DGF 123, Miracle Power Products) and allowed to dry at room temperature for 5 min.[2] Prior to measurement, all samples were equilibrated at $298\ K$. For compressed pellets of THDBT fillers, the penetration model was used for data analysis and thermal diffusivity extraction.

Specific heat capacity measurements.

Specific heat capacities are measured using differential scanning calorimetry (DSC 2500, TA Instruments). Measurements are conducted from $273\ to\ 323\ K$ at a heating rate of $10\ ^{\circ}C\ minute^{-1}$. Each DSC run consisted of four heating–cooling cycles; the first cycle is used to remove the sample's thermal history, and the subsequent three cycles are used to determine the specific heat capacity. Approximately $6-9\ mg$ of samples is used per measurement. Nitrogen is employed as the purge gas at a flow rate of $300\ mL\ minute^{-1}$. Film samples prepared in Section S1 are cut into circular specimens ($6.7\ mm$ in diameter) using a hollow punch.

Density measurements by Archimedes' principle.

The densities of pure PU films, PU/THDBT hybrids, and compressed pellets of THDBT fillers are determined using Archimedes' principle. *n*-hexane is used as the immersion medium. Approximately $0.5\ g$ of each sample was placed in a graduated cylinder, followed by the addition of 5 mL of *n*-hexane. The mixture was allowed to settle for $10\ minutes$, and the increase in liquid volume corresponded to the sample volume. Each measurement was repeated three times to obtain an average density value for each sample.[2]

^{13}C solid-state nuclear magnetic resonance (NMR) analysis.

A saturation-recovery experiment was conducted to study the ^{1}H T_1 relaxation of each constituent in the samples. Saturation was achieved by a train of sixteen ^{1}H 90° pulses spaced by 1 ms delays, followed by a variable recovery period ranging between $50\ ms$ and $30\ s$, then followed by a ^{1}H 90° excitation, ^{1}H-to-^{13}C cross polarization (CP) and ^{13}C detection with ^{1}H decoupling. The experiments were performed under magic angle spinning (MAS) on a Bruker 600 MHz solid-state NMR spectrometer in a $4\ mm$ broadband-observe CP/MAS probe. A spinning speed of $9\ kHz$, contact time of $2\ ms$, a recycle delay of $5\ s$, and a decoupling field strength of $60\ kHz$ were used for NMR experiments. Chemical shift was calibrated by setting the unprotonated aromatic carbon signal of 1,4-di(t-butyl)benzene at 148.8 ppm.

Synchrotron X-ray scattering measurement.

Wide-angle and small-angle X-ray scattering (WAXS/SAXS) experiments were performed at the Complex Materials Scattering (CMS, 11-BM) beamline at the National Synchrotron Light Source II (NSLS-II), Brookhaven National Laboratory. Samples are mounted in a custom-designed static holder configured for transmission geometry. X-rays with an energy of $13.5\ keV$ ($\lambda \approx 0.918\ \text{Å}$) are used. Scattering patterns are collected with Pilatus 2M (SAXS) and Pilatus 800K (WAXS) detectors positioned at sample-to-detector distances of $\sim 5\ m$ and $\sim 0.26\ m$, respectively. The incident beam size is approximately $0.2\ mm \times 0.2\ mm$. Background subtraction was carried out using scattering data from the empty holder. Two-dimensional scattering images are azimuthally integrated using the SciAnalysis software package to obtain one-dimensional $I(q)$ versus q profiles. The exposure time for each measurement is $30\ s$.

Attenuated total reflectance Fourier transform infrared (ATR-FTIR) spectroscopy analysis.

The ATR-FTIR spectroscopy is performed using a PerkinElmer Spectrum One FT-IR spectrometer. Spectra are recorded in the range of $4000 - 550\ cm^{-1}$ with a resolution of $2\ cm^{-1}$. To improve the signal-to-noise ratio, each sample is scanned ten times, and the averaged spectrum is used for analysis. All measurements are conducted at $298\ K$ under ambient conditions.

Confocal micro-Raman microscopy measurements

Confocal micro-Raman microscopy measurements were performed using a 532 nm excitation laser in a backscattering geometry, with a laser power of 5 mW and an integration time of 10 s. For each spectrum, 10 individual acquisitions were averaged. The baseline subtraction was applied. The high scattering intensity of THDBT leads to an increased background signal, which is the primary source of spectral noise.

Microscale combustion calorimeter analysis.

The microscale combustion calorimeter analysis was performed according to the ASTM D7309-21, method A,[3] using an $80\ cm^{3}\ min^{-1}$ stream of N2(g) and a heating rate of $1\ {}^{\circ}C\ s^{-1}$. In the microscale combustion calorimeter, the anaerobic thermal degradation products were combined with a $20\ cm^{3}\ min^{-1}$ stream of oxygen gas in a furnace at $900\ {}^{\circ}C$. Key flammability parameters, including heat release capacity, fire growth capacity, and total heat release were calculated from experimental data.[4-6]

Heat release capacity quantifies the maximum heat release rate normalized by the mass loss rate during combustion and serves as a reliable indicator of a material's intrinsic flammability, largely dictated by its chemical structure and degradation behavior (Figure 4B).[1,7] Fire growth capacity provides a broader evaluation by incorporating both combustibility and ignitability, especially reflecting how rapidly a polymer contributes to fire growth following ignition (Figure 4C).[1,7] Together, heat release capacity and fire growth capacity offer complementary metrics that enable a comprehensive assessment of flammability in polymer materials.

Section S2.2 Error analysis.

Population standard deviation and error propagation analyses of thermal diffusivity, specific heat capacity, density, and thermal conductivity were performed according to previous publications.[2]

Section S3. Molecular dynamics simulations of thermal transport in polymer/filler hybrids.

Section 3.1 Molecular dynamics simulations – methodology.

Atomistic molecular dynamics (MD) simulations were conducted to evaluate the interfacial thermal resistance and specific heat capacity of the PU/THDBT hybrids. All simulations were performed using LAMMPS[8] and structural visualization was carried out with OVITO.[9]

Three simulation systems were considered in this study: pure PU, pure THDBT, and the PU–THDBT interface as shown in Figure S7(A), (C)and (E)respectively. The total number of atoms in these systems was 5610, 4950, and 4986, respectively. The atomic configurations were generated under the assumption that each polymer was in a purely amorphous state. The polymer consistent force field (PCFF) was employed, with a time step of $0.5\ fs$. Each system was first equilibrated for 1 ns under the NPT ensemble at $298\ K$ and $1\ atm$. After NPT relaxation, the simulation box dimensions were $2.60\ \times\ 2.602\ \times\ 8.21\ nm$ for PU, $2.41\ \times\ 2.41\ \times\ 8.75\ nm$ for THDBT, and $2.67\ \times\ 2.67\ \times\ 7.45\ nm$ for the PU/THDBT interface.

Section 3.2 Determination of interfacial thermal resistance and thermal conductivity

A highly localized section of the PU/THDBT matrix was extracted to model the interfacial region. Two PU/THDBT interfaces were constructed by placing a THDBT layer between two PU regions, as illustrated in **Figure S7 (E)**. The interfacial thermal resistance was evaluated using the non-equilibrium molecular dynamics (NEMD) approach. For this purpose, the simulation domain along the z-axis was partitioned into multiple regions. Total $0.22\ nm$ layer at each end of the simulation box was designated as a fixed region, where atomic forces and velocities were set to zero, thereby rendering the system aperiodic along the z-direction. Periodic boundary conditions were applied in the x and y directions. Adjacent to the left and right fixed regions, $5.5\ nm$ zones were defined as the heat source and heat sink, respectively, for imposing the thermal gradient. The system was first equilibrated under the NVT ensemble for 1 ns, after which it was switched to the NVE ensemble. In the NVE stage, heat was continuously supplied to the source region and removed from the sink region at a constant rate of $17.36\ nJ\ s^{-1}$. This heating–cooling process was maintained for 6 ns, until the average temperatures of the source and sink reached a steady state, as shown in **Figure S7 (G)**. The simulation box was then divided into 40 equally spaced slabs along the z-direction, and the temperature and density of each slab were computed and averaged over an additional 1 ns. The resulting spatial variations in density and temperature are presented in **Figure S7 (H)** and **Figure 3B** in the main text respectively, and are hereafter referred to as the density and temperature profiles. The positions of the interfaces were identified by visual inspection of these profiles, corresponding to abrupt changes in both density and temperature. The interfaces were located at $2.93\ nm$ and $5.68\ nm$ from the origin along the z-axis, as indicated by the dotted vertical lines in **Figure 3B** of the main text. To quantify the temperature discontinuity across the interfaces, linear fits were applied to the temperature profile within the three distinct regions (PU, THDBT, and PU), and the temperature drops were extracted from the intersections of these fitted lines with vertical lines of the interfaces, as illustrated in **Figure 3B** of the main text. The interfacial thermal resistance (ITR) was calculated using equation S3-Eq1 in this supplementary materials file.

$$ITR = \frac{\Delta T A}{\dot{Q}} \quad \text{(S3-Eq1)}$$

where ΔT is the temperature drops across the interface, A is the cross-sectional area of the xy-plane perpendicular to the heat-transfer direction, and $\dot{Q}$ is the heat rate supplied to the source or removed from the sink.

A similar procedure was employed to determine the thermal conductivity of the pure PU and pure THDBT systems. In this case, instead of measuring the interfacial temperature drop, the slope of the fitted linear segment in the temperature profile (data not shown) was obtained. The thermal conductivity was then calculated using Fourier's law of heat conduction as expressed in Equation S3-Eq2.

$$\kappa = - \frac{\dot{Q}}{A\frac{dT}{dz}} \quad \text{(S3-Eq2)}$$

Where, κ is thermal conductivity, $\dot{Q}$ is heat rate applied to heat source or removed from the heat sink, A is the xy plane cross-sectional area and $\frac{dT}{dz}$ is the slope of the temperature profile along heat transfer direction.

Section 3.3 Determination of specific heat capacity.

The specific heat capacities of pure PU and pure THDBT were determined from their vibrational density of states (VDOS). To obtain the VDOS, atomic velocities were recorded under the NVE ensemble with a sampling interval of $4\ fs$ over a total simulation time of $500\ ps$. The VDOS was calculated by performing a Fourier transform of the velocity time series for each velocity components, followed by computing the mass-weighted average magnitude of the transformed velocities across all atoms. The computed VDOS spectra was normalized such that the total area under the curve equaled to unity. The mathematical formulation for the computation of VDOS is expressed in Equations S3-Eq3 through *S3-Eq5*.[10,11]

$$\hat{v}_p(\omega) = \int_{-\infty}^{\infty} v_p(t)\, e^{-i\omega t} dt \quad \text{(S3-Eq3)}$$

$$g(\omega) = \frac{A}{N_{atom}} \sum_{i=1}^{Natom} m_i \sum_{p=1}^{3} [\hat{v}_p(\omega) \times \hat{v}_p^{\,*}(\omega)] \quad \text{(S3-Eq4)}$$

$$\int g(\omega)\, d\omega = 1 \quad \text{(S3-Eq5)}$$

Where, g is the normalized magnitude of VDOS, ω is angular frequency, A is the normalization prefactor, $v_p\,(p = 1,2,3)$ $is\ the\ velocity\ components\ of\ an\ atom\ i\ (i = 1,2,...Natom)$, m is the mass of the atom, N_{atom} is the total number of atoms in the system and t denotes time.

Finally, specific heat was calculated from Equation S3-Eq6.[11,12]

$$C_v(T) = \frac{3N_{atoms}k_b}{m_{system}} \int \left(\frac{\hbar\omega}{k_bT}\right)^2 \frac{\exp\left(\frac{\hbar\omega}{k_bT}\right)}{\left[\exp\left(\frac{\hbar\omega}{k_bT}\right) - 1\right]^2} g(\omega) d\omega \quad \text{(S3-Eq6)}$$

Where, C_v is the specific heat at constant volume, k_b is the Boltzmann constant, $\hbar$ is reduced Planck's constant, T is the temperature, m_{system} is the total mass of the system and N_{atom} is the total number of atoms in the system.

Section 3.4 Results and discussion

Computed density of PU and THDBT after NPT relaxation at $298\,K$ temperature and 1 atm pressure are $0.94\ g\ cm^{-3}$ and $1.24\ g\ cm^{-3}$Density of THDBT is higher than PU which follows the experimental trends where experimental values are $1.095\ g\ cm^{-3}$ and $1.15\ g\ cm^{-3}$, respectively.

Thermal conductivity of pure PU and THDBT from the simulation are $0.206\ W\,m^{-1}\,K^{-1}$ and $0.199\ W\,m^{-1}\,K^{-1}$, which also follows the experimental trends but does not match the experimental values.

Interfacial thermal resistances (R_{ITR}) at two interfaces are $0.5 \times 10^{-9}\ and\ 1.1 \times 10^{-9}\ m^2\ K\ W^{-1}$respectively which corresponds to $1.49\,K$ and $2.97\,K$ temperature drop at interface. Average R_{ITR} is $0.80 \times 10^{-9}\ m^2\ K\ W^{-1}$. These values suggest that there is very low thermal resistance between PU and THDBT.

Although the simulation results follow the experimental trends, they do not exactly match the experimental values. Several factors may contribute to these discrepancies. First, in the MD simulations, PU was modeled as an amorphous phase, whereas in the experiments PU exhibits a predominantly amorphous structure with hard-segment ordering. Second, there is a size effect: in MD simulations, only a highly localized (nanoscale) portion of the material is modeled, and it is well established that thermal properties are size-dependent at this scale. The combined influence of these factors leads to deviations from experimental values, even though the simulations can reliably predict the overall experimental trends.

Section 4 Applicability and limitations of effective medium theory for THDBT/PU hybrids

To quantitatively assess whether effective medium theory (EMT) can describe thermal transport in PU/THDBT hybrids, we carried out a systematic EMT analysis using standard formulations, including Nan-type models.[13]

All experimentally accessible structural and material parameters were independently determined in Section 4, leaving only the intrinsic filler (THDBT) thermal conductivity and the interfacial thermal resistance as adjustable parameters.

Section 4.1 Structural and materials parameters

Small-angle X-ray scattering (SAXS) and solid-state NMR consistently indicate THDBT aggregates with a characteristic domain size of approximately 21 nm (**Figures. 5C** and **5A** in the manuscript). Wide-angle X-ray scattering (WAXS) yields an orientational order parameter $\langle \cos^2\theta \rangle \approx 0.33$, suggesting an isotropic dispersion of the THDBT fillers within polymer matrices (**Figure 5B** in this submitted manuscript and **Figure S1** in this supplementary materials).[2] The absence of q^{-1} or q^{-2} power-law regimes in SAXS (**Figure 5C**) unambiguously excludes rod-like or platelet-like morphologies of THDBT aggregates.[14] Accordingly, the THDBT aggregates were simply modeled as low–aspect-ratio ellipsoids with semi-axes $a_1 \approx 13$nm, $a_2 \approx 10$nm, and $a_3 \approx 24$nm, estimated from the lowest-energy conformation generated using 3D ChemDraw.[15,16] The measured thermal conductivity of neat polyurethane ($k_{polymer}$, ~0.14 W m^{-1} K^{-1}) was used as the polymer matrix thermal conductivity. This measured $k_{polymer}$ value is consistent with previously reported values.[2,13,17-20]

Section 4.2 EMT formulation and fitting strategy

All experimentally accessible structural and material parameters were independently determined in Section 4.1, such that only the intrinsic filler thermal conductivity (k_{filler}) and the interfacial thermal resistance (R_{ITR}) remained as adjustable parameters.[2,13]

Within the EMT framework,[13] interfacial resistance effects are incorporated through the Kapitza length (l_K), defined as

$$l_K = R_{ITR}\, k_{filler} \quad (Equation\ S4 - Eq1).$$

where R_{ITR} denotes the matrix–filler interfacial thermal resistance and $k_{filler}$is the thermal conductivity of the filler. This defination renormalizes the effective inclusion response.[13]

In $Equation\,S4 - Eq1$, R_{ITR} represents the interfacial thermal resistance at the filler–polymer matrix interface, and k_{filler} denotes the intrinsic thermal conductivity of the filler phase.

The governing dimensionless parameter, which compares the Kapitza length to the characteristic inclusion size (a_1 of THDBT aggregates),[13] is therefore expressed as Equation S4-Eq2

$$\frac{l_K}{a_1} = \frac{R_{ITR}\,k_{filler}}{a_1}\;(Equation\,S4 - Eq2)$$

Like discussion above, for the measured THDBT filler geometry and polymer matrix properties, only the intrinsic filler thermal conductivity k_{filler} and the interfacial thermal resistance R_{ITR} at the filler-polymer matrix interface are the only remaining fitting parameters.[2,13]

Section 4.3 Intrinsic non-uniqueness of EMT fits

As shown in **Figure S8**, fitting the measured effective thermal conductivity $k_{eff}(\phi)$ yields significant **non-uniqueness**. Parameter sets differing by nearly two orders of magnitude—$R_{ITR} = 10^{-9}\,m^2K\,W^{-1}$ with $k_{filler} = 0.378\,W\,m^{-1}K^{-1}$ (**Figure S8A**) and $R_{ITR} = 10^{-7}\,m^2K\,W^{-1}$ with $k_{filler} = 0.0569\,W\,m^{-1}K^{-1}$ (**Figure S8B**)—produce essentially indistinguishable agreement with experiment.

This non-uniqueness is intrinsic to EMT, as interfacial thermal resistance R_{ITR} does not enter as an independent parameter but only through the combined quantity $\frac{l_K}{a_1}$. As a result, variations in R_{ITR} can be offset by corresponding changes in k_{filler}, preventing unique identification of R_{ITR} from bulk EMT fitting, particularly for nanoscale fillers with low thermal conductivity on the order of $0.1\,W\,m^{-1}\,K^{-1}$ or lower.

Section 4.4 Physical inapplicability of EMT to the PU/THDBT hybrid system

1) For nanoscale THDBT filler aggregates with characteristic dimensions $a_1 \approx 13$ nm, $a_2 \approx 10$ nm, and $a_3 \approx 24nm$, physically realistic interfacial thermal resistances ($R_{ITR} \lesssim 10^{-8}\,m^2\,K\,W^{-1}$) correspond to a small Kapitza length $l_K = R_{ITR}k_m$, such that $l_K/a_1 \ll 1$.[13] This places the system in a perturbative regime in which interfacial effects are intrinsically weak and enter only as higher-order corrections. In this limit, EMT remains mathematically valid but exhibits **little sensitivity** to interfacial thermal transport. Even when $R_{ITR}$is increased to $\sim 10^{-7}\,10^{-8}\,m^2\,K\,W^{-1}$, such that $l_K/a_1 \sim O(1)$, EMT does not acquire enhanced sensitivity to interfacial heat-transfer mechanisms. Instead, it predicts a saturation behavior in which nanoscale THDBT aggregates behave as effectively insulating inclusions, such that effective heat transport is dominated by pathways through the polymer matrix. Consequently, further increases in R_{ITR}lead to only marginal changes in the effective thermal conductivity. [13]
2) When the intrinsic thermal conductivity of the THDBT filler is low (k_{filler} on the order of 0.1 W m^{-1}K^{-1} or lower), heat transport within disordered nanoscale THDBT aggregates becomes spatially

heterogeneous and bottleneck-controlled, with heat flux preferentially bypassing low-conductivity regions. Under such conditions, describing the filler phase by a single, spatially averaged thermal conductivity is no longer physically well defined, which challenges the uniform-inclusion assumption underlying effective medium theory.

Taken together, these considerations indicate that, for the present PU/THDBT hybrid system, there is no parameter regime in which EMT can simultaneously remain valid and explicitly capture interfacial heat-transfer physics.

Section 4.5 Implications

Taken together, this analysis demonstrates that effective medium theory (EMT) is **not** applicable to describing thermal transport physics in PU/THDBT hybrids, including interfacial thermal transport study and interfacial thermal resistance calculation (R_{ITR}). This inapplicability arises from the nanoscale THDBT aggregate size ($a_1 \approx 13$nm, $a_2 \approx 10$nm, and $a_3 \approx 24$nm), low intrinsic conductivity (k_{filler} $on\ the\ order\ of$ $0.1\ W\,m^{-1}K^{-1}$ or lower), and disordered internal structures of the THDBT aggregates, rather than from insufficient data or unconstrained fitting parameters.

As a result, EMT **cannot** be used to validate interfacial heat-transfer mechanisms in this PU/THDBT system, consistent with the mechanistic interpretation advanced in the main text.

Section S5. Effective Hamiltonian model for polymer thermal transport with fillers.

Section 5.1 Hamiltonian model setup for a polymer chain.

We consider the 1D polymer chain, with monomers and their on-site monomer energy ε_A and inter-monomer hopping t_A, the pristine polymer's (PU) vibrational Hamiltonian can be written as

$$H_{\mathrm{PU}} = \sum_j \varepsilon_A a_j^+ a_j - t_A \sum_j (a_j^+ a_{j+1} + \mathrm{h.c.}) \tag{S5-Eq1}$$

where for simplicity, we neglect the hard/soft segments, but only treat PU as a uniform polymer, and the standard Bosonic commutation relation $[a_i, a_j^+] = \delta_{ij}$ applies. After Fourier transform $a_k = \frac{1}{\sqrt{N}} \sum_{j=1}^{N} e^{-ikaj} a_j$ (with inter-monomer spacing *a*), the pristine polymer's vibrational Hamiltonian can be diagonalized as

$$H_{\mathrm{PU}} = \sum_k \left[\varepsilon_A - 2t_A \cos ka\right] a_k^+ a_k \tag{S5-Eq2}$$

Now, the fire-retardant THDBT blocks (termed as "B") are randomly distributed in the polymer chain with a filling fraction *c*. We treat such monomer-THDBT composite as binary alloy system, with both diagonal, on-site disorder as well as off-diagonal disorder from hopping. The composite Hamiltonian can be written as

$$H = \sum_j \varepsilon_j a_j^+ a_j - \sum_j t_{j,j+1}(a_j^+ a_{j+1} + \text{h.c.}) \tag{S5-Eq3}$$

where $\varepsilon_j \in \{\varepsilon_A, \varepsilon_B\}$, $t_{j,j+1} \in \{t_{AA}, t_{BB}, t_{AB}\}$. Here "A" denotes the original monomers with concentration 1-*c*, and "B" denotes the THDBT blocks with concentration *c*.

Section 5.2 BEB-coherent potential approximation.

To proceed, we adopt the coherent-potential approximation (CPA) with an extension off-diagonal disorder, i.e. disorder from the hopping. This is the so-called Blackman-Esterling-Berk (BEB) formalism as a generalization of CPA.[21] The effective "coherent" Hamiltonian H_0, which serves as a background effective medium, can be written as

$$\begin{aligned} H_0 &= \sum_j \varepsilon_{\text{coh}}(\omega) a_j^+ a_j - t_{\text{coh}}(\omega) \sum_j (a_j^+ a_{j+1} + \text{h.c.}) \\ &= \sum_k \left(\varepsilon_{\text{coh}}(\omega) - 2t_{\text{coh}}(\omega)\cos ka\right) a_k^+ a_k \end{aligned} \tag{S5-Eq4}$$

To apply CPA, which uses the coherent medium to approximate the alloy system, we need to remove the site *j* in the coherent medium and later re-insert the real monomer or THDBT blocks. We can divide the space from the local site "*j*" part and the rest "environment" excluding site *j*, called $\bar{j}.\{\bar{j}\} = 1, 2, ..., j-1, j+1, ...N.$. The inverse CPA Green's function can be written as

$$G_0^{-1}(\omega) = \omega - H_0 = \begin{pmatrix} \omega - \varepsilon_{\text{coh}}(\omega) & T \\ T^+ & \left[G_0^{\bar{j}}(\omega)\right]^{-1} \end{pmatrix} \tag{S5-Eq5}$$

where the (1,1) block is the Hamiltonian for site *j,* T is a 1 x (*N*-1) row vector $T = t_{\text{coh}}(\omega)\left(|j-1\rangle + |j+1\rangle\right)$with i^{th} component$T_i = \langle i|\omega - H_0|j\rangle = t_{\text{coh}}(\omega)\left(\delta_{i,j-1} + \delta_{i,j+1}\right), i \in \{\bar{j}\}$, and $G_0^{\bar{j}}(\omega) = \dfrac{1}{\omega I - H_0^{\bar{j}}}$ is the "cavity Green's function" that excludes the site *j* and other couplings with site *j*.

The local Green's function $G_{0,jj}(\omega)$ at site *j* can be computed using Schur complement as

$$\begin{aligned} G_{0,jj}(\omega) &= \langle j|G_0(\omega)|j\rangle = \langle j|\frac{1}{\omega - H_0}|j\rangle \\ &= \left(\omega - \varepsilon_{\text{coh}}(\omega) - TG_0^{\bar{j}}(\omega)T^+\right)^{-1} \\ &= \frac{1}{\omega - \varepsilon_{\text{coh}}(\omega) - t_{\text{coh}}^2(\omega)R(\omega)} \end{aligned} \tag{S5-Eq6}$$

in which

$$\begin{aligned} R(\omega) &= \langle j-1 | G_0^{\bar{j}}(\omega) | j-1 \rangle + \langle j+1 | G_0^{\bar{j}}(\omega) | j+1 \rangle \\ &= \frac{a}{2\pi} \int dk \frac{\sin^2 ka}{\omega - \varepsilon_{\text{coh}}(\omega) + 2t_{\text{coh}} \cos ka} \\ &= \frac{(\omega - \varepsilon_{\text{coh}}) - \sqrt{(\omega - \varepsilon_{\text{coh}})^2 - 4t_{\text{coh}}^2}}{t_{\text{coh}}^2} \end{aligned} \tag{S5-Eq7}$$

is the "cavity return," aka the environmental propagator "seen" when going one step away and return to site *j*. The term $t_{\text{coh}}^2(\omega)R(\omega)$ is the local self-energy to quantify how the "environment" (rest of the system excluding *j*) can impact the site *j* in effective medium.

As a sanity check, with translational invariance, we can also first obtain the energy-momentum space Green's function

$$G_0(k,\omega) = \frac{1}{\omega - \varepsilon_{\text{coh}}(\omega) + 2t_{\text{coh}}(\omega)\cos ka + i0^+} \tag{S5-Eq8}$$

After Fourier transform, we have the real-space, on-site Green's function written as

$$\begin{aligned} G_{0,jj}(\omega) &= \frac{a}{2\pi} \int G_0(k,\omega) dk = \frac{a}{2\pi} \int_{-\pi/a}^{+\pi/a} \frac{1}{\omega - \varepsilon_{\text{coh}}(\omega) + 2t_{\text{coh}}(\omega)\cos ka + i0^+} dk \\ &= \frac{1}{\sqrt{(\omega - \varepsilon_{\text{coh}}(\omega))^2 - 4t_{\text{coh}}^2(\omega)}} \end{aligned} \tag{S5-Eq9}$$

which gives the same results as Eqs. *(S4-Eq6) and (S4-Eq7)* before. The CPA local density-of-states can then be written as

$$\rho(\omega) = -\frac{1}{\pi} \operatorname{Im} G_{0,jj}(\omega + i0^+) \tag{S5-Eq10}$$

Now we replace the coherent background at local site *j* with actual monomer A or filler B, and the environment stays the same. The local Green's function, when ensuring single-site locality, can be written as

$$G_{\sigma,jj}(\omega) = \frac{1}{\omega - \varepsilon_\sigma(\omega) - t_{\sigma\sigma}^2 R(\omega)}, \sigma = \text{A}, \text{B} \tag{S5-Eq11}$$

Then, defining the single-site effective scattering potential vertex at site A or B as,

$$V_\sigma(\omega) = \varepsilon_\sigma - \varepsilon_{\text{coh}}(\omega) + \left(t_{\sigma\sigma}^2 - t_{\text{coh}}^2(\omega)\right) R(\omega), \sigma = \text{A}, \text{B} \tag{S5-Eq12}$$

we can write down the Dyson's equation

$$G_{\sigma,jj}(\omega)=G_{0,jj}(\omega)+G_{0,jj}(\omega)V_{\sigma}(\omega)G_{\sigma,jj}(\omega) \tag{S5-Eq13}$$

Similarly, the single-site T-matrix can be written as

$$\begin{aligned} T_{\mathrm{A}}(\omega)&=\frac{V_{\mathrm{A}}(\omega)}{1-V_{\mathrm{A}}(\omega)G_{0,jj}(\omega)} \\ T_{\mathrm{B}}(\omega)&=\frac{V_{\mathrm{B}}(\omega)}{1-V_{\mathrm{B}}(\omega)G_{0,jj}(\omega)} \end{aligned} \tag{S5-Eq14}$$

Finally, we can impose the CPA self-consistent condition, at each frequency,

$$(1-c)T_{\mathrm{A}}(\omega)+cT_{\mathrm{B}}(\omega)=0 \tag{S5-Eq15}$$

Physically, this means that replacing the coherent effective medium to real local site does not lead to additional scattering. Besides vanishing site-scattering, we also have the bonding scattering condition, i.e.,

$$(1-c)\frac{t_{AA}^{2}-t_{\mathrm{coh}}^{2}(\omega)}{1-V_{\mathrm{A}}(\omega)G_{0,jj}(\omega)}+c\frac{t_{BB}^{2}-t_{\mathrm{coh}}^{2}(\omega)}{1-V_{\mathrm{B}}(\omega)G_{0,jj}(\omega)}=0 \tag{S5-Eq16}$$

if we subtract Eq. (16) from(15), we have:

$$(1-c)\frac{\varepsilon_{A}-\varepsilon_{\mathrm{coh}}(\omega)}{1-V_{\mathrm{A}}(\omega)G_{0,jj}(\omega)}+c\frac{\varepsilon_{B}-\varepsilon_{\mathrm{coh}}(\omega)}{1-V_{\mathrm{B}}(\omega)G_{0,jj}(\omega)}=0 \tag{S5-Eq17}$$

which is the average energy condition, highlighting that the effective coherent medium does not change the averaged energy.

Section 4.3 Heat capacity and thermal conductivity.

Since the trend of thermal conductivity and specific heat capacity are the same as a function of filler fraction, according to the recent work,[2]

$$C_{V}(T)=\int_{0}^{+\infty}d\omega\frac{\omega^{2}e^{\beta\omega}}{T^{2}(e^{\beta\omega}-1)^{2}}\rho(\omega) \tag{S5-Eq18}$$

Similarly, we can do thermal conductivity,

$$\begin{aligned} k(T)&=\frac{1}{T}\int_{0}^{+\infty}d\omega\omega^{2}\left(-\frac{\partial n_{B}}{\partial\omega}\right)\frac{a}{2\pi}\int_{-\pi/a}^{+\pi/a}dkv_{k}^{2}(\omega)\left[A_{0}(k,\omega)\right]^{2} \\ v_{k}(\omega)&=\partial_{k}\left(\varepsilon_{\mathrm{coh}}(\omega)-2t_{\mathrm{coh}}(\omega)\cos ka\right)=2a\sin ka \end{aligned} \tag{S5-Eq19}$$

in which $A_{0}(k,\omega)=-\frac{1}{\pi}\mathrm{Im}\,G_{0}(k,\omega)$ is the spectral function of the CPA Green's function Eq. *(S4-Eq8)*.

We also summarize the brief procedure to use CPA to compute the thermal conductivity in a disordered polymer:

1) Obtain energies from MD/DFT calculation, including ε_A, ε_B, t_{AA}, and t_{BB} as fitting parameters. Set $t_{AB} = \sqrt{t_{AA} t_{BB}}$.
2) Pick a filler fractional concentration $0 < c < 1$, substitute back to the BEB-CPA equations *Eq. (S4-Eq15) and Eq. (S4-Eq17)*, to obtain the CPA parameters $\varepsilon_{\mathrm{coh}}(\omega)$ and $t_{\mathrm{coh}}(\omega)$.
3) Use *Eq. (S4-Eq9)* to compute CPA local DOS $\rho(\omega)$, and use *Eq. (S4-Eq8)* to compute CPA spectral function $A_0(k,\omega)$.
4) Use *Eq. (S4-Eq18) and (S4-Eq19)* to compute heat capacity and thermal conductivity.

Figures. S1 to S10

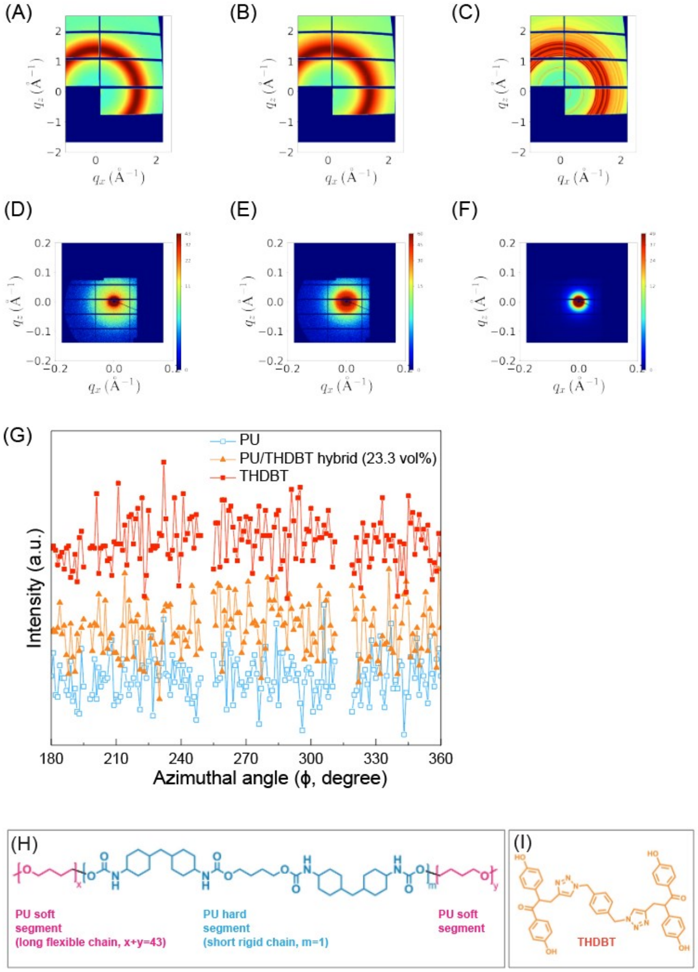

Figure. S1. Structural characterizations using synchrotron X-ray scattering. (A) Wide-angle X-ray scattering patterns of pure PU thin film. **(B)** Wide-angle X-ray scattering patterns of PU/THDBT hybrid ($23.3\ vol\%$) thin film. **(C)** Wide-angle X-ray scattering patterns of compressed pellets of THDBT fillers. **(D)** Small-angle X-ray scattering patterns of pure PU thin film. **(E)** Small-angle X-ray scattering patterns of pure PU thin film PU/THDBT hybrid ($23.3\ vol\%$) thin film. **(F)** Small-angle X-ray scattering patterns of compressed pellets of THDBT fillers. **(G)** Azimuthal line cuts integrated around the peak ($q = 1.374$ Å^{-1}) within a ± 0.006 Å^{-1} width of the PU in pure PU film. Azimuthal line cuts integrated around the peak ($q = 1.400$ Å^{-1}) within a ± 0.006 Å^{-1} width of the THDBT in PU/THDBT hybrid ($23.3\ vol\%$). Azimuthal line cuts integrated around the peak ($q = 1.400$ Å^{-1}) within a ± 0.006 Å^{-1} width of the THDBT in compressed pellets of THDBT fillers. **(E)** Chemical structures of THDBT containing benzene rings and triazole rings. **(C)** Chemical structures of PU with hard and soft segments.

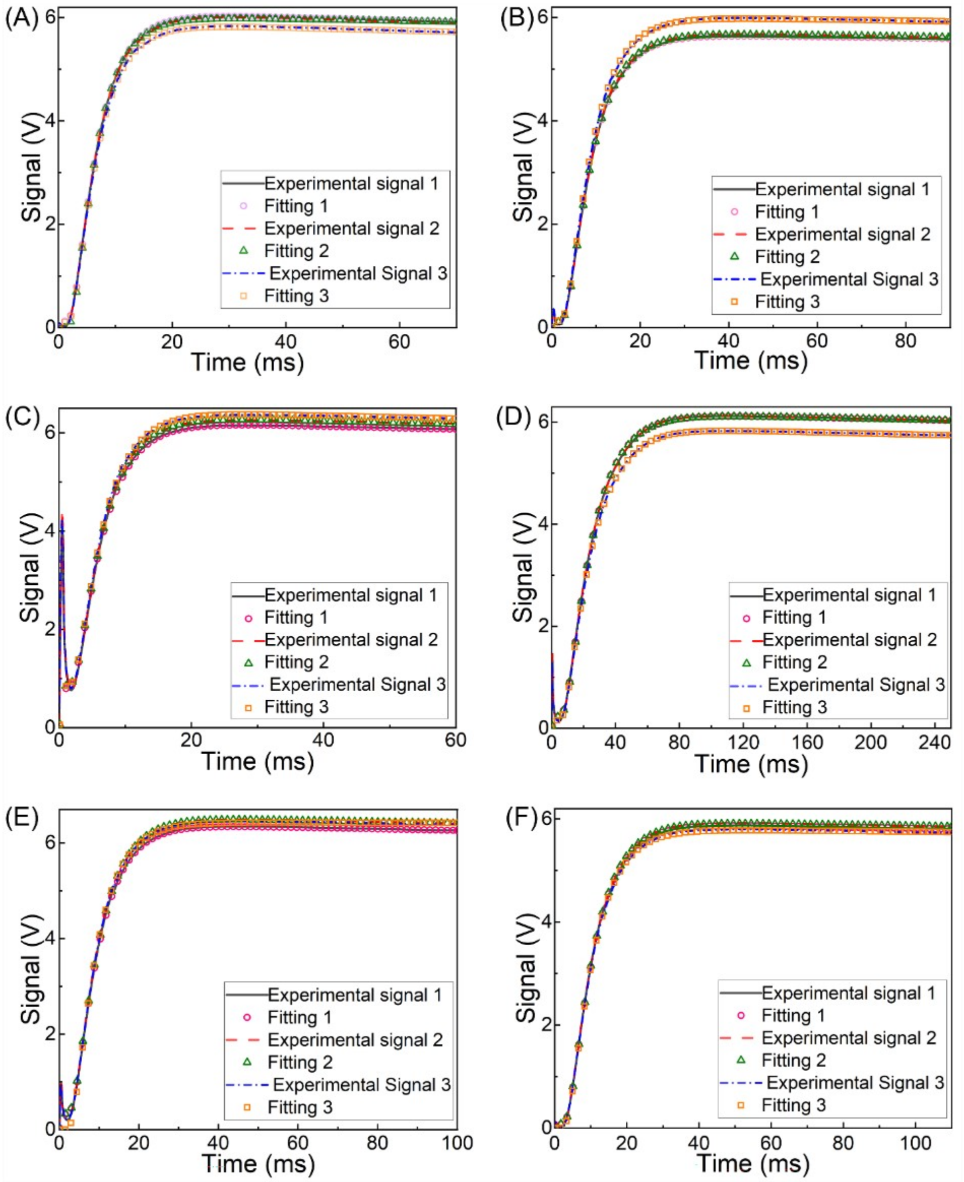

Figure S2. Measured cross-plane thermal diffusivities of pure PU thin films. In order to minimize random errors and ensure the reproducibility of thermal diffusivity experimental measurements made using the laser flash method, each sample was tested three times. Thermal diffusivity results of 6 different PU thin films are shown. All samples were coated with graphite spray (DGF 123) on both sides before thermal diffusivity testing. The "transparent" model in the LFA 467 software was used to fit the crossplane thermal diffusivity experimental signals obtained from the laser flash method. **(A)** Experimental and fitting results for cross-plane thermal diffusivities of thin film (PU) with a thickness of $0.0547\ mm$. **(B)** Experimental and fitting results for cross-plane thermal diffusivities of thin film (PU) with a thickness of $0.0680\ mm$. **(C)** Experimental and fitting results for cross-plane thermal diffusivities of thin film (PU) with a thickness of $0.0590\ mm$. **(D)** Experimental and fitting results for cross-plane thermal diffusivities of thin film (PU) with a thickness of $0.1140\ mm$. **(E)** Experimental and fitting results for cross-plane thermal diffusivities of thin film (PU) with a thickness of $0.0665\ mm$. **(F)** Experimental and fitting results for cross-plane thermal diffusivities of thin film (PU) with a thickness of $0.0720\ mm$.

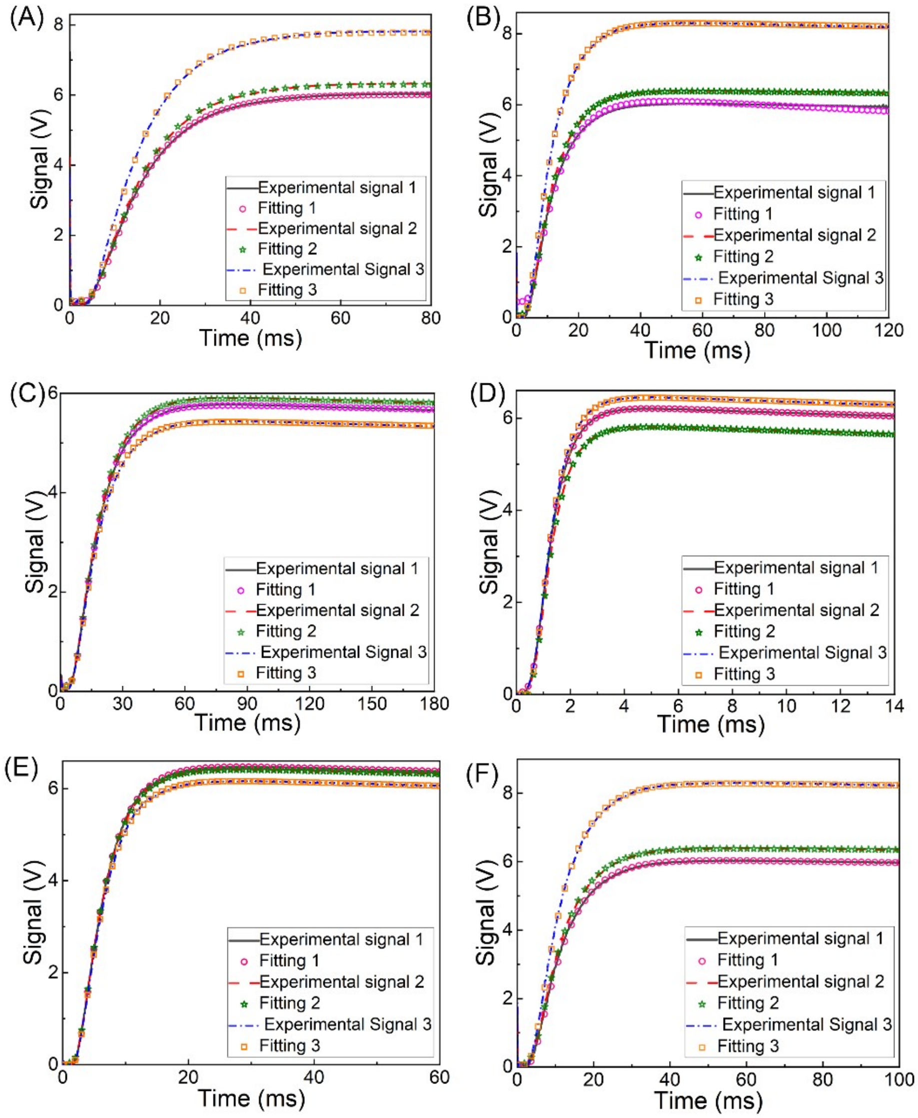

Figure S3. Measured cross-plane thermal diffusivities of PU/THDBT hybrids (4.5 vol%). In order to minimize random errors and ensure the reproducibility of thermal diffusivity experimental measurements made using the laser flash method, each sample was tested three times. Thermal diffusivity results of 6 different PU/THDBT hybrids ($4.5\ vol\%$) are shown. All samples were coated with graphite spray (DGF 123) on both sides before thermal diffusivity testing. The "transparent" model in the LFA 467 software was used to fit the cross-plane thermal diffusivity experimental signals obtained from the laser flash method. **(A)** Experimental and fitting results for cross-plane thermal diffusivities of thin film (PU/THDBT hybrids ($4.5\ vol\%$)) with a thickness of $0.0715\ mm$. **(B)** Experimental and fitting results for cross-plane thermal diffusivities of thin film (PU/THDBT hybrids ($4.5\ vol\%$) with a thickness of $0.0750\ mm$. **(C)** Experimental and fitting results for cross-plane thermal diffusivities of thin film(PU/THDBT hybrids ($4.5\ vol\%$)) with a thickness of $0.0940\ mm$. **(D)** Experimental and fitting results for cross-plane thermal diffusivities of thin film (PU/THDBT hybrids (4.5 vol%) with a thickness of $0.0225\ mm$. **(E)** Experimental and fitting results for cross-plane thermal diffusivities of thin film (PU/THDBT hybrids ($4.5\ vol\%$)) with a thickness of $0.0535\ mm$. **(F)** Experimental and fitting results for cross-plane thermal diffusivities of thin film (PU/THDBT hybrids ($4.5\ vol\%$)) with a thickness of $0.0850\ mm$.

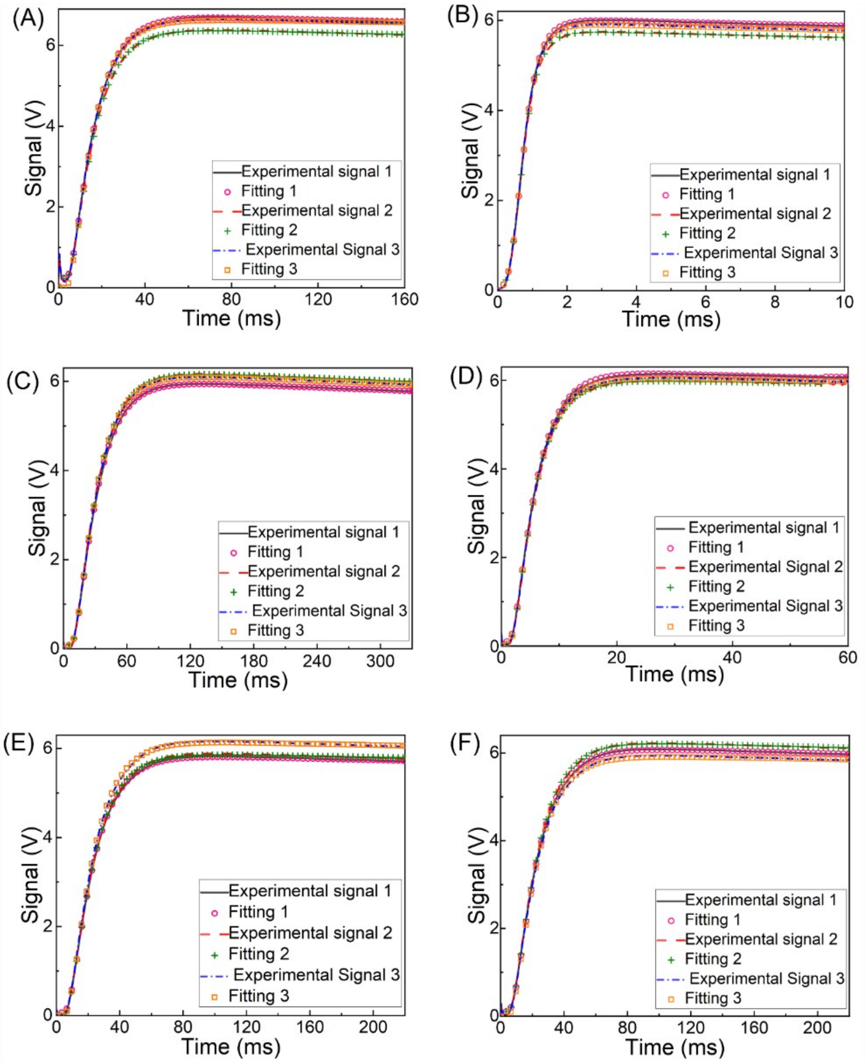

Figure. S4. Measured cross-plane thermal diffusivities of PU/THDBT hybrids ($13.9\ vol\%$). In order to minimize random errors and ensure the reproducibility of thermal diffusivity experimental measurements made using the laser flash method, each sample was tested three times. Thermal diffusivity results of 6 different PU/THDBT $13.9\ vol\%$ hybrid samples are shown. All samples were coated with graphite spray (DGF 123) on both sides before thermal diffusivity testing. The "transparent" model in the LFA 467 software was used to fit the crossplane thermal diffusivity experimental signals obtained from the laser flash method. **(A)** Experimental and fitting results for cross-plane thermal diffusivities of thin film (PU/THDBT hybrids ($13.9\ vol\%$)) with a thickness of $0.0870\ mm$. **(B)** Experimental and fitting results for cross-plane thermal diffusivities of thin film (PU/THDBT hybrids ($13.9\ vol\%$)) with a thickness of $0.1320\ mm$. **(C)** Experimental and fitting results for cross-plane thermal diffusivities of thin (PU/THDBT hybrids (13.9 vol%)) with a thickness of $0.0560\ mm$. **(D)** Experimental and fitting results for cross-plane thermal diffusivities of thin film (PU/THDBT hybrids ($13.9\ vol\%$)) with a thickness of $0.1050\ mm$. **(E)** Experimental and fitting results for cross-plane thermal diffusivities of thin film (PU THDBT Hybrid (PU/THDBT hybrids ($13.9\ vol\%$)) with a thickness of $0.1030\ mm$. **(F)** Experimental and fitting results for cross-plane thermal diffusivities of thin film (PU/THDBT hybrids ($13.9\ vol\%$)) with a thickness of $0.1040\ mm$.

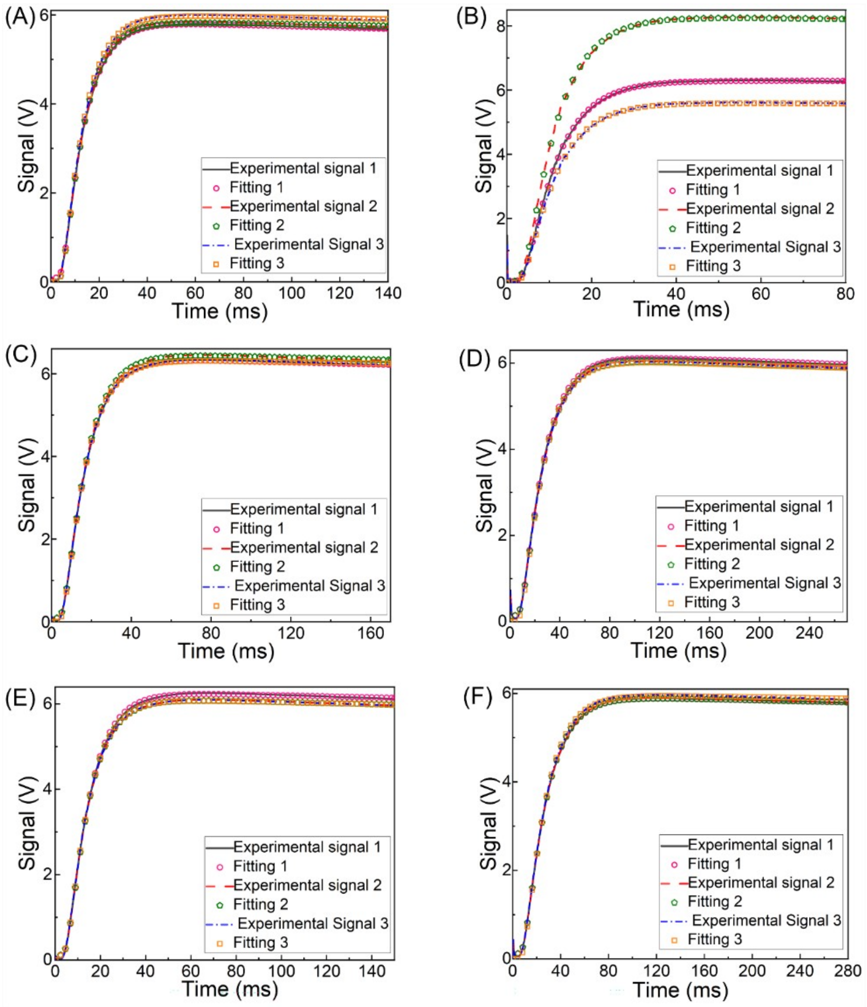

Figure. S5. Measured cross-plane thermal diffusivities of PU/THDBT hybrids ($23.3\ vol\%$). In order to minimize random errors and ensure the reproducibility of thermal diffusivity experimental measurements made using the laser flash method, each sample was tested three times. Thermal diffusivity results of 6 different PU/THDBT 23.3 vol% hybrid samples are shown. All samples were coated with graphite spray (DGF 123) on both sides before thermal diffusivity testing. The "transparent" model in the LFA 467 software was used to fit the crossplane thermal diffusivity experimental signals obtained from the laser flash method. **(A)** Experimental and fitting results for cross-plane thermal diffusivities of thin film (PU/THDBT hybrids ($23.3\ vol\%$)) with a thickness of $0.0800\ mm$. **(B)** Experimental and fitting results for cross-plane thermal diffusivities of thin film (PU/THDBT hybrids ($23.3\ vol\%$)) with a thickness of $0.0770\ mm$. **(C)** Experimental and fitting results for cross-plane thermal diffusivities of thin film (PU/THDBT hybrids ($23.3\ vol\%$)) with a thickness of $0.0870\ mm$. **(D)** Experimental and fitting results for cross-plane thermal diffusivities of thin film (PU/THDBT hybrids ($23.3\ vol\%$)) with a thickness of $0.1160\ mm$. **(E)** Experimental and fitting results for cross-plane thermal diffusivities of thin film (PU/THDBT hybrids ($23.3\ vol\%$)) with a thickness of $0.0810\ mm$. **(F)** Experimental and fitting results for cross-plane thermal diffusivities of thin film (PU/THDBT hybrids ($23.3\ vol\%$)) with a thickness of $0.1165\ mm$.

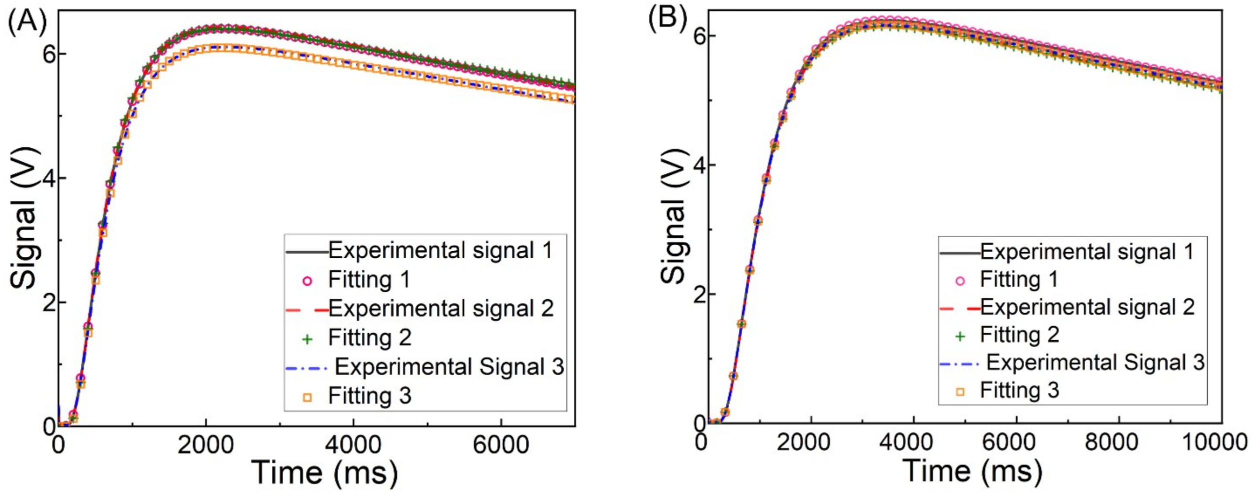

Figure S6. Measured cross-plane thermal diffusivities of compressed pellets of THDBT fillers. In order to minimize random errors and ensure the reproducibility of the thermal diffusivity experimental measurements made using the laser flash method, each sample was tested three times. Thermal diffusivity results of 2 different THDBT samples are shown. All samples were coated with graphite spray (DGF 123) on both sides before thermal diffusivity testing. The "penetration" model in the LFA 467 software was used to fit the crossplane thermal diffusivity experimental signals obtained from the laser flash method. **(A)** Experimental and fitting results for cross-plane thermal diffusivities of compressed pellets of THDBT fillers with thickness of $1.1550\ mm$. **(B)** Experimental and fitting results for cross-plane thermal diffusivities of compressed pellets of THDBT fillers with thickness of $0.9560\ mm$.

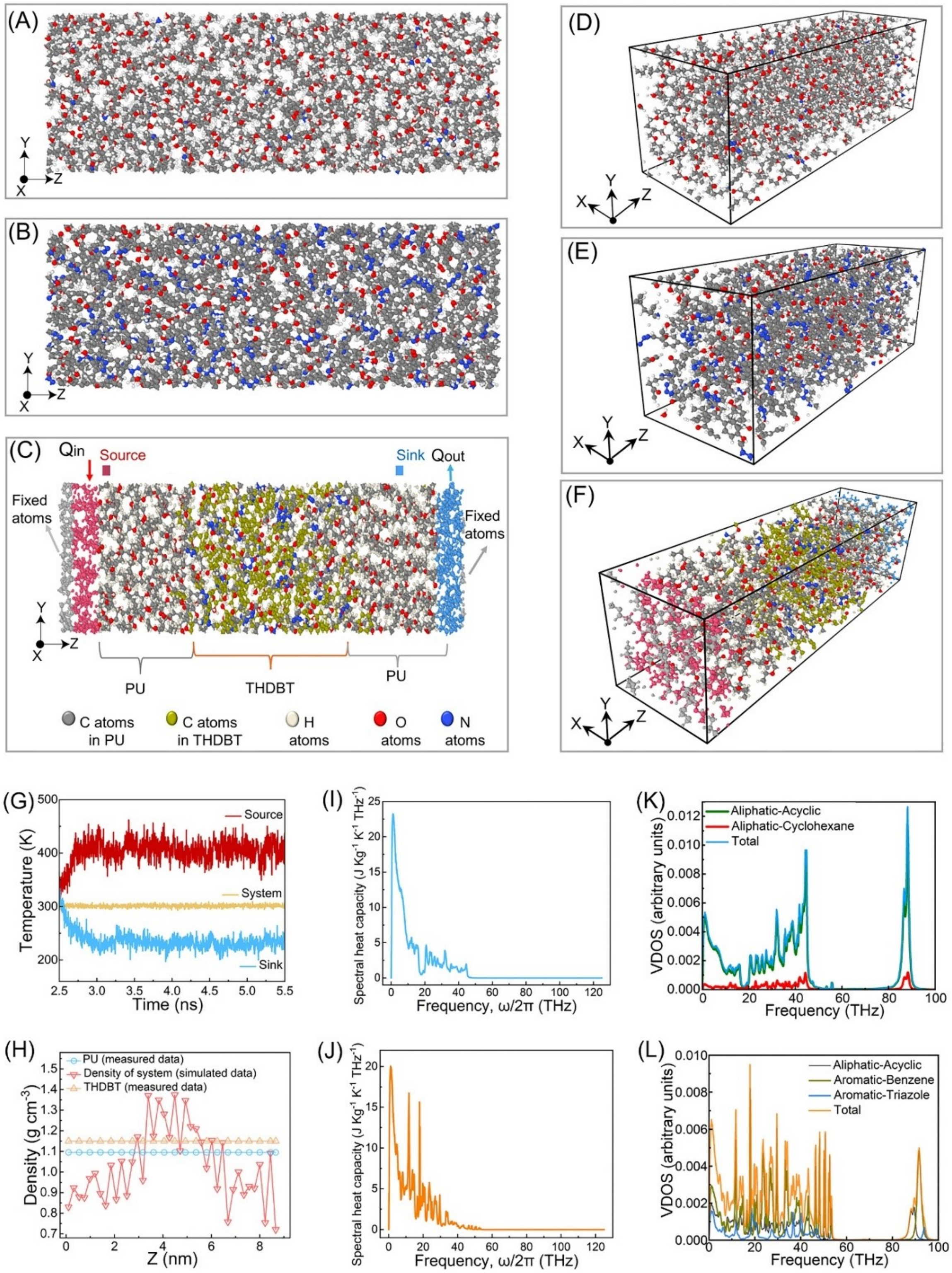

Figure S7. **(A)** Simulation domain of PU. **(B)** Simulation domain of THDBT. **(C)** Simulation domain of PU/THDBT interface. **(D)** Three-dimensional view of simulation domain of PU. **(E)** 3-dimensional view of simulation domain of THDBT. **(F)** Three-dimensional view of simulation domain of PU/THDBT interface. **(G)** Temperature of heat source, heat sink and overall temperature of the system with time. The average temperature of the heat source and sink becomes steady after 3.5 ns. **(H)** Density of the system at different positions along the z axis. **(I)** Spectral heat capacity of PU **(J)** Spectral heat capacity of THDBT. **(K)** the vibrational density of states (VDOS) contributions from different chain segments of PU. **(L)** the vibrational density of states (VDOS) contributions from different functional groups of THDBT.

For clarity, in Figures S7K and S7L, the polymer backbones are divided into four segments based on chemical configuration: (i) Aromatic benzene, consisting of C and H atoms in the benzene ring; (ii) Aromatic triazole, consisting of C, H, and N atoms in the triazole ring, (iii) Aliphatic acyclic backbone, consisting of C, H, and O atoms; and (iv) Aliphatic cyclic backbone, consisting of C, H of cyclohexene. A distinct contrast is observed in the $45 - 55\,THz$ frequency range, where THDBT exhibits pronounced peaks that are absent in PU. In this region, the dominant contribution arises from the benzene ring vibrations of THDBT. The presence of these high-frequency phonon modes shifts the overall VDOS of THDBT toward higher frequencies relative to PU. Consequently, the phonon population in the $20 - 40\,THz$ range is reduced. This results in a lower specific heat capacity for THDBT compared to PU As only lower frequency modes ($< 45\,THz$) contribute to heat capacity.

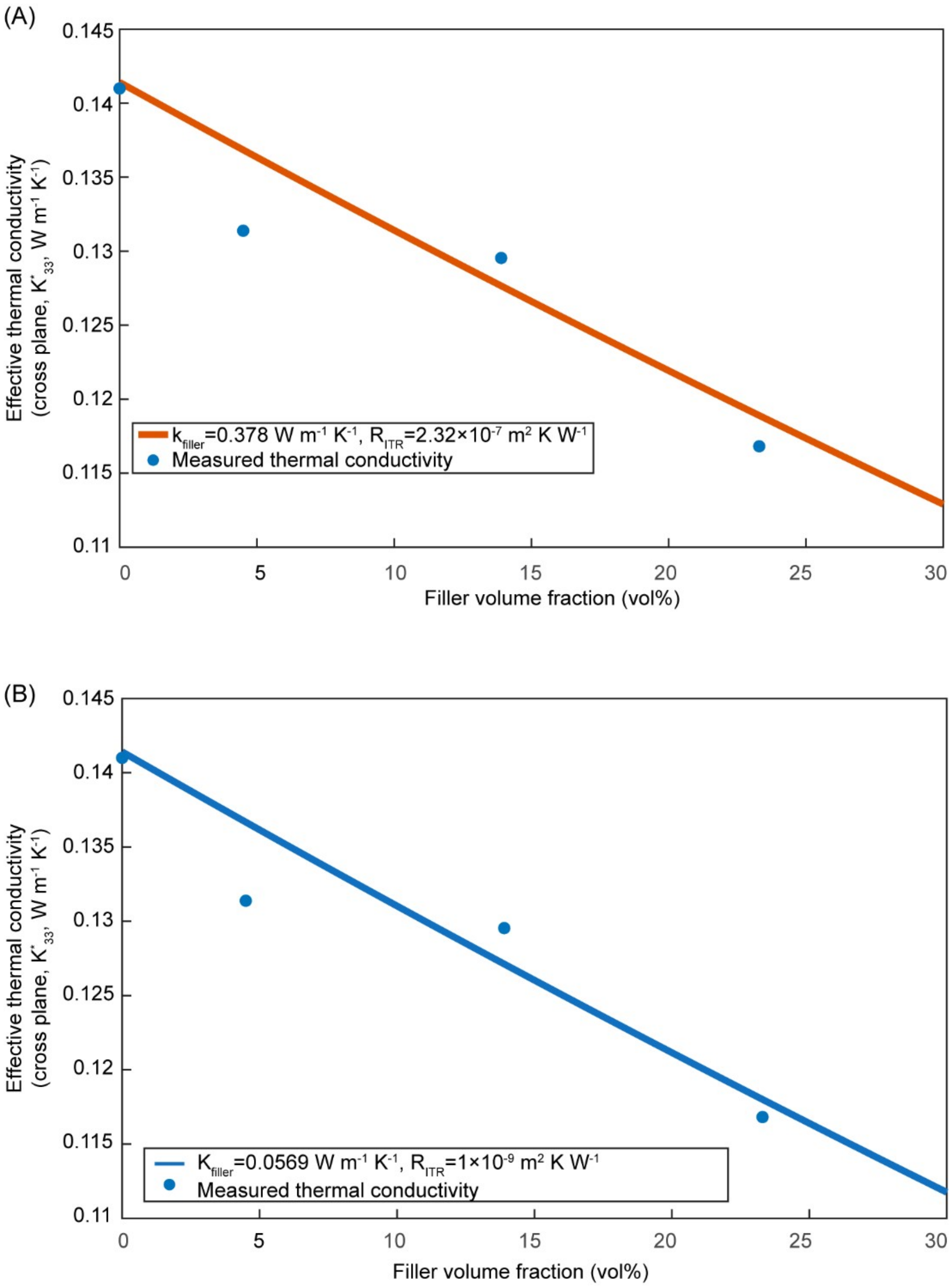

Figure S8. **Effective medium theory fits to the measured cross-plane thermal conductivity of PU/THDBT hybrids.** Symbols represent experimental data, while solid lines denote EMT predictions obtained using two distinct parameter sets: **(A)** $R_{ITR} = 10^{-9}\, m^2\, K\, W^{-1}$, $k_{filler} = 0.378\, W\, m^{-1}\, K^{-1}$; and **(B)** $R_{ITR} = 10^{-7}\, m^2\, K\, W^{-1}$, $k_{filler} = 0.0569\, W\, m^{-1}\, K^{-1}$. Despite the orders-of-magnitude difference in R_{ITR}, both parameter sets yield comparable agreement with the experimental data, demonstrating that EMT fits to bulk thermal conductivity alone cannot uniquely determine R_{ITR} in this system.

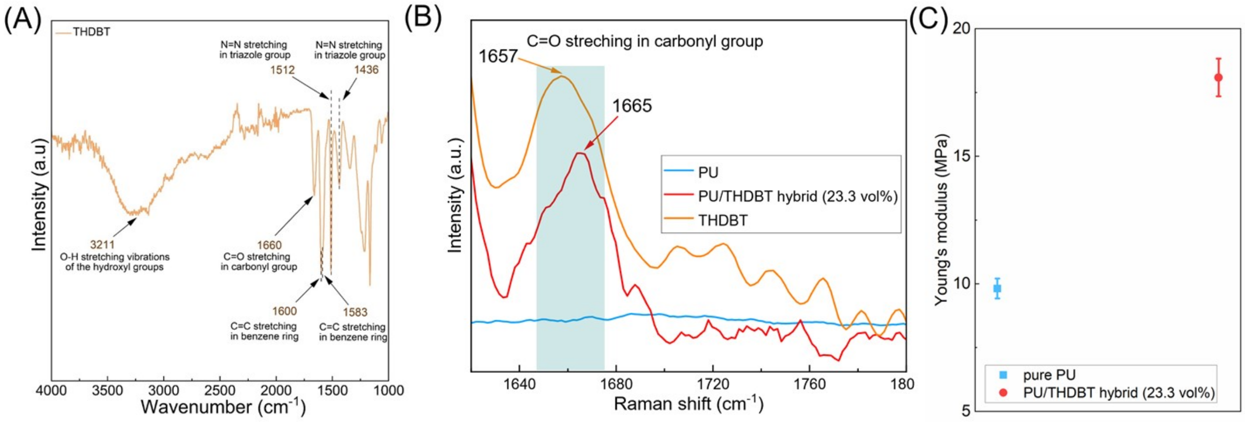

Figure S9. (**A**) ATR-FTIR spectra of compressed pellets made from THDBT. Please note that ATR-FTIR spectrum for THDBT in Figure 6D, because the O–H stretching vibrations in pure THDBT are much weaker than the N–H stretching vibrations in pure PU, the O–H peaks ($\sim 3211\ cm^{-1}$) appears flattened when all ATR-FTIR spectra are plotted together. For clarity, the individual ATR-FTIR spectrum of pure THDBT is shown in this Figure S8. (**B**) Raman spectra of PU, PU/THDBT hybrid ($23.3\ vol\%$), and THDBT powder. **(C)** Young's modulus properties of pure PU and PU/THDBT hybrid ($23.3\ vol\%$).

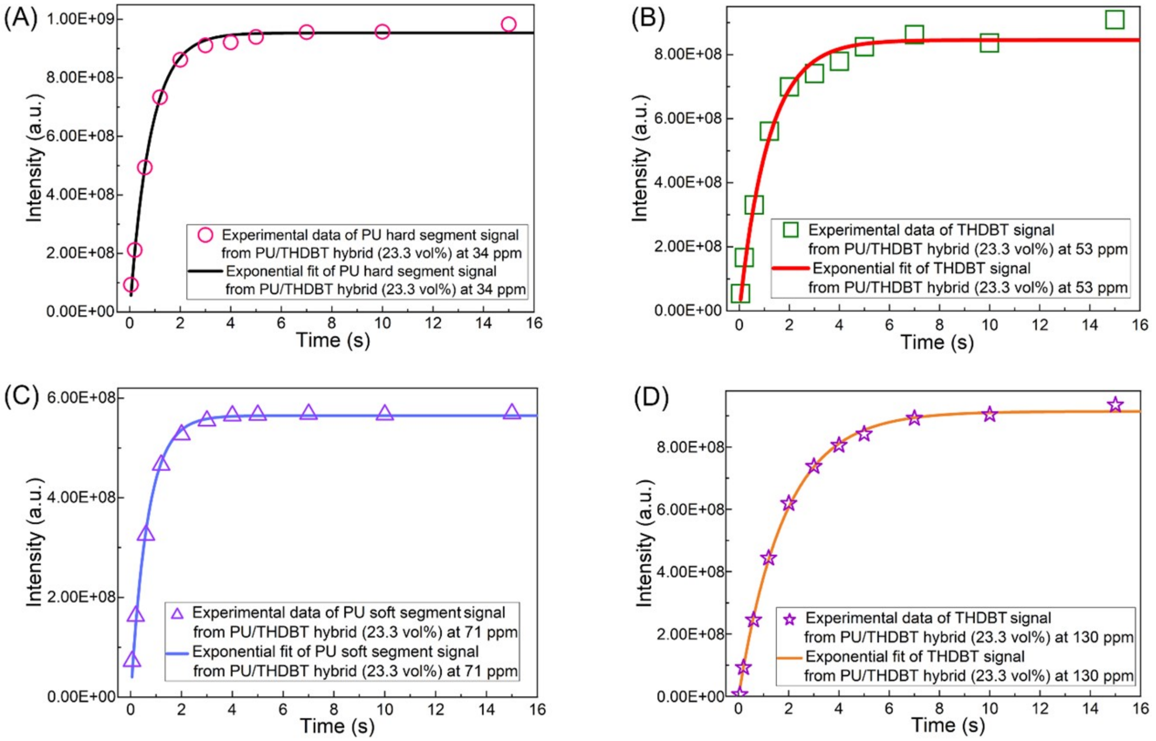

Figure S10. ^{1}H T1 recovery curves for PU/THDBT hybrid ($23.3\ vol\%$). Intensity is shown in arbitrary units (a.u.). (A) Polyurethane (PU) hard segment signal at 34 ppm from PU/THDBT hybrid ($23.3\ vol\%$). (B) THDBT signal at $53\ ppm$ from PU/THDBT hybrid ($23.3\ vol\%$). (C) PU soft segment signal at $71\ ppm$ from PU/THDBT hybrid ($23.3\ vol\%$). (D) THDBT signal at $130\ ppm$ from PU/THDBT hybrid ($23.3\ vol\%$).

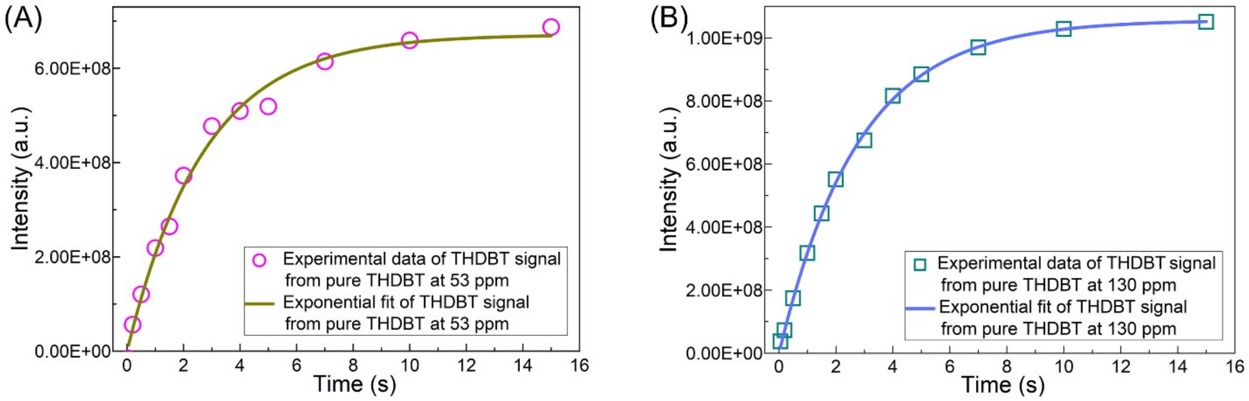

Figure. S11. ^{1}H T1 recovery curves for pure THDBT. Intensity is shown in arbitrary units (a.u.). **(A)** THDBT signal at $53\ ppm$ from pure THDBT. **(B)** THDBT signal at $130\ ppm$ from pure THDBT.

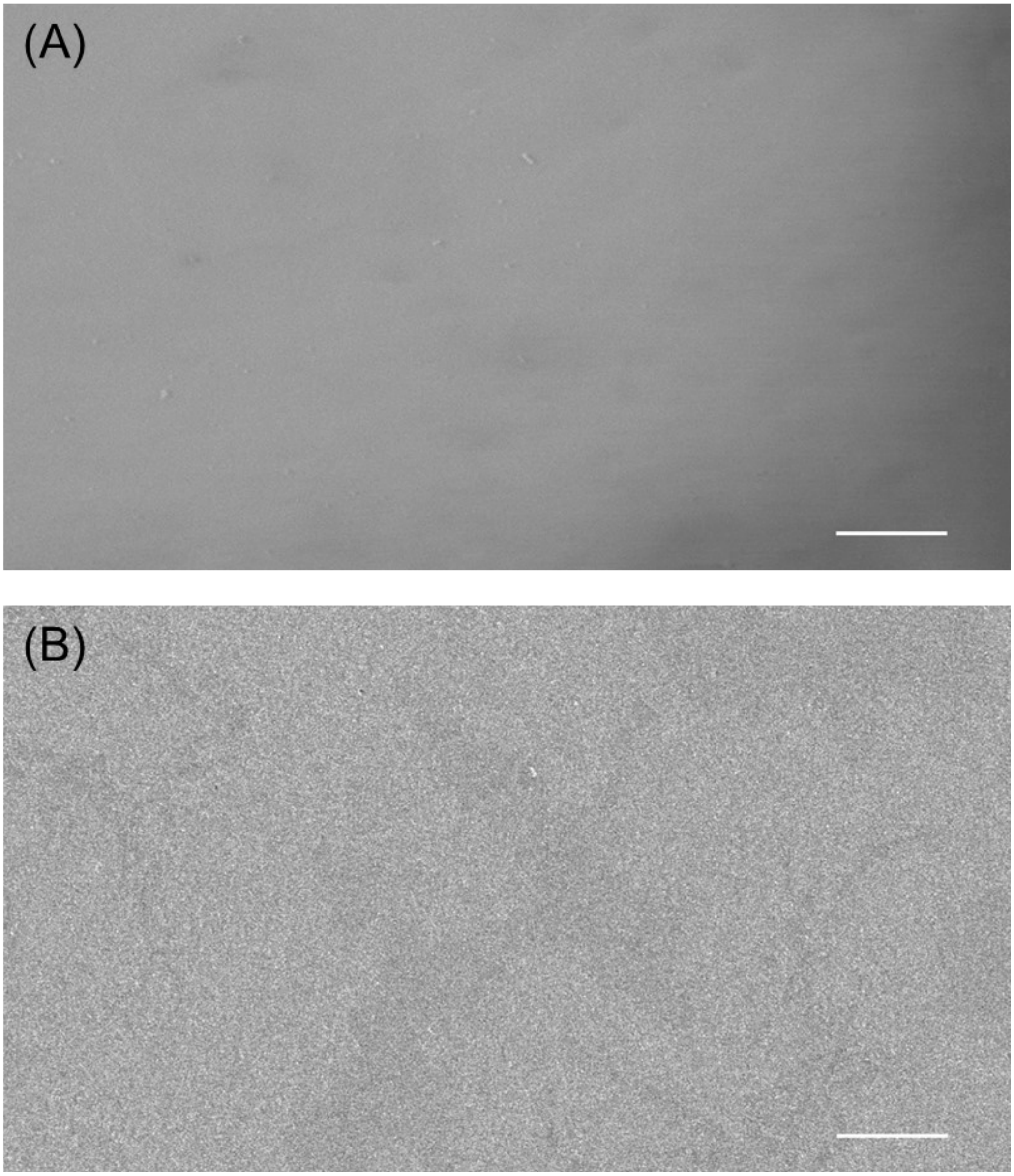

Figure S12. (A) SEM image of pure PU films (scale bar: 1 μm) and **(B)** SEM image of PU/THDBT hybrid films (23.3 vol%; scale bar: 20 μm). In this context, the term *nonporous in the title* is used to indicate the absence of **mesoscopic or nanoscale porosity associated with phase separation, void formation, or solvent residues**, rather than the complete absence of molecular-scale free volume.

Table S1. Comparison of representative dense and porous low-thermal-conductivity polymer systems reported in the literature and the present PU/THDBT hybrids.

Polymer Material System	Dense / Porous	Thermal conductivity (k, W m^{-1} K^{-1})	Reference
Representative dense polymers (e.g., polystyrene and PMMA)	Dense	~0.10–0.20	Thermal Conductivity of Polymers and Their Nanocomposites[22]
Fluorinated polyurethanes	Dense	~0.13	Reduction of the Thermal Conductivity of Polyurethanes by Fluorination: Impact of Crystallinity, Atomic Density, and Sound Velocity[17]
PCBM/fullerene-based materials	Dense	~0.03–0.06	Ultralow thermal conductivity of fullerene derivatives[23]
Polyurethane foam	Porous (>95% porosity)	~0.023–0.026	Porous Thermal Insulation Polyurethane Foam Materials [24]
Present PU/THDBT hybrids	Dense	~0.117	This work.

Table S2. ^{1}H T1 relaxation times (s).

	PU Soft segments	PU hard segments	THDBT
PU/THDBT hybrid films with a THDBT volume fraction of $23.3\ vol\%$	$0.67 \pm 0.03\ (s)$	$0.82 \pm 0.03\ (s)$	$1.83 \pm 0.04\ (s)$
THDBT	not applicable	not applicable	$2.78 \pm 0.05\ (s)$

References

1 K. Munusamy, C.-H. Chen & T. Emrick. Alkyne-Substituted Deoxybenzoins as Precursors to Cycloaddition Chemistry and the Preparation of Low-Flammability Polymers and Blends. *Macromolecules* (2023) **56**, 9237–9247, https://doi.org/10.1021/acs.macromol.3c01737

2 Y. Zhou, R. Ciarla, A. Boonkird, S. Raza, T. Nguyen, J. Zhou, N. C. Osti, E. Mamontov, Z. Jiang, X. Zuo, J. Ranasinghe, W. Hu, B. Scott, J. Chen, D. K. Hensley, S. Huang, J. Liu, M. Li & Y. Xu. Defects Vibrations Engineering for Enhancing Interfacial Thermal Transport in Polymer Composites. *Science Advances* (2025) **11**, eadp6516, https://doi.org/10.1126/sciadv.adp6516

3 C. Q. Yang, Q. He, R. E. Lyon & Y. Hu. Investigation of the Flammability of Different Textile Fabrics Using Micro-Scale Combustion Calorimetry. *Polymer Degradation and Stability* (2010) **95**, 108–115, https://doi.org/10.1016/j.polymdegradstab.2009.11.047

4 Q. Xu, R. A. Mensah, C. Jin & L. Jiang. A Critical Review of the Methods and Applications of Microscale Combustion Calorimetry for Material Flammability Assessment. *Journal of Thermal Analysis and Calorimetry* (2022) **147**, 6001–6013, https://doi.org/10.1007/s10973-021-10963-4

5 M. Li, Z. Han, L. Jiang & Q. Xu. Investigating Correlations between Thermogravimetric Analysis and Microscale Combustion Calorimetry in Polymer Studies. *Journal of Thermal Analysis and Calorimetry* (2025) **150**, 11845–11857, https://doi.org/10.1007/s10973-024-13975-y

6 R. A. Mensah, Q. Xu, S. Asante-Okyere, C. Jin & G. Bentum-Micah. Correlation Analysis of Cone Calorimetry and Microscale Combustion Calorimetry Experiments. *Journal of Thermal Analysis and Calorimetry* (2019) **136**, 589–599, https://doi.org/10.1007/s10973-018-7661-5

7 R. E. Lyon. Heat Release Kinetics. *Fire and Materials* (2000) **24**, 179–186, https://doi.org/10.1002/1099-1018(200007/08)24:4%3C179::AID-FAM736%3E3.0.CO;2-V

8 A. P. Thompson, H. M. Aktulga, R. Berger, D. S. Bolintineanu, W. M. Brown, P. S. Crozier, P. J. in 't Veld, A. Kohlmeyer, S. G. Moore, T. D. Nguyen, R. Shan, M. J. Stevens, J. Tranchida, C. Trott & S. J. Plimpton. Lammps - a Flexible Simulation Tool for Particle-Based Materials Modeling at the Atomic, Meso, and Continuum Scales. *Computer Physics Communications* (2022) **271**, 108171, https://doi.org/10.1016/j.cpc.2021.108171

9 A. Stukowski. Visualization and Analysis of Atomistic Simulation Data with Ovito–the Open Visualization Tool. *Modelling and Simulation in Materials Science and Engineering* (2010) **18**, 015012, https://doi.org/10.1088/0965-0393/18/1/015012

10 M. P. Allen & D. J. Tildesley. *Computer Simulation of Liquids*. (Oxford university press, 2017).

11 A. Giri, A. Z. Chen, A. Mattoni, K. Aryana, D. Zhang, X. Hu, S.-H. Lee, J. J. Choi & P. E. Hopkins. Ultralow Thermal Conductivity of Two-Dimensional Metal Halide Perovskites. *Nano Letters* (2020) **20**, 3331–3337, https://doi.org/10.1021/acs.nanolett.0c00214

12 M. Kaviany. *Heat Transfer Physics*. (Cambridge University Press, 2014).

13 C.-W. Nan, R. Birringer, D. R. Clarke & H. Gleiter. Effective Thermal Conductivity of Particulate Composites with Interfacial Thermal Resistance. *Journal of Applied Physics* (1997) **81**, 6692–6699, https://doi.org/10.1063/1.365209

14 L. Feigin & D. I. Svergun. *Structure Analysis by Small-Angle X-Ray and Neutron Scattering*. Vol. 1 (Springer, 1987).

15 Z. Li, H. Wan, Y. Shi & P. Ouyang. Personal Experience with Four Kinds of Chemical Structure Drawing Software: Review on Chemdraw, Chemwindow, Isis/Draw, and Chemsketch. *Journal of Chemical Information and Computer Sciences* (2004) **44**, 1886–1890, https://doi.org/10.1021/ci049794h

16 J. Raiyn & A. Rayan. How Chemicals' Drawing and Modeling Improve Chemistry Teaching in Colleges of Education. *World Journal of Chemical Education* (2015) **3**, 1–4, https://pubs.sciepub.com/wjce/3/1/1/

17 J. Zhou, C. Chen, J. Sun, T. R. Fielitz, W. Zhou, D. G. Cahill & P. V. Braun. Reduction of the Thermal Conductivity of Polyurethanes by Fluorination: Impact of Crystallinity, Atomic Density, and Sound Velocity. *Angewandte Chemie International Edition* (2025) **64**, e202503497, https://doi.org/10.1002/anie.202503497

18 D. Mani, M. C. Vu, C.-S. Lim, J.-B. Kim, T.-H. Jeong, H. J. Kim, M. A. Islam, J.-H. Lim, K.-M. Kim & S.-R. Kim. Stretching Induced Alignment of Graphene Nanoplatelets in Polyurethane Films for Superior in-Plane Thermal Conductivity and Electromagnetic Interference Shielding. *Carbon* (2023) **201**, 568–576, https://doi.org/10.1016/j.carbon.2022.09.047

19 P. Rutkowski, K. Kwiecień, A. Berezicka, J. Sułowska, A. Kwiecień, K. Śliwa-Wieczorek, B. Azinovic, M. Schwarzkopf, A. Pondelak, J. G. Pečnik & M. Szumera. Thermal Stability and Heat Transfer of Polyurethanes for Joints Applications of Wooden Structures. *Molecules* (2024) **29**, 3337, https://doi.org/10.3390/molecules29143337

20 J. Zhou, X. Li, C. Chen, W. Zhou, T. R. Fielitz, P. V. Braun & D. G. Cahill. Thermal Conductivity of Polyurethane Thin Films. *Macromolecules* (2024) **57**, 6838–6847, https://doi.org/10.1021/acs.macromol.4c00401

21 J. A. Blackman, D. M. Esterling & N. F. Berk. Generalized Locator---Coherent-Potential Approach to Binary Alloys. *Physical Review B* (1971) **4**, 2412–2428, https://doi.org/10.1103/PhysRevB.4.2412

22 X. Xu, J. Chen, J. Zhou & B. Li. Thermal Conductivity of Polymers and Their Nanocomposites. *Advanced Materials* (2018) **30**, 1705544, https://doi.org/10.1002/adma.201705544

23 X. Wang, C. D. Liman, N. D. Treat, M. L. Chabinyc & D. G. Cahill. Ultralow Thermal Conductivity of Fullerene Derivatives. *Physical Review B* (2013) **88**, 075310, https://https://link.aps.org/doi/10.1103/PhysRevB.88.075310

24 Z. G. Wang, C. Z. Wang, Y. B. Gao, Z. Li, Y. Shang & H. F. Li. Porous Thermal Insulation Polyurethane Foam Materials. *Polymers* (2023) **15**, 3818, https://doi.org/10.3390/polym15183818